X-BAND AOM ON CHIP

Hao Tian¹, Junqiu Liu², Anat Siddharth², Blésin Terence²,

Tobias J. Kippenberg², and Sunil A. Bhave¹

OxideMEMS Lab, Purdue University, West Lafayette, IN, USA

Institute of Physics, Swiss Federal Institute of Technology Lausanne (EPFL), Lausanne,

Switzerland

ABSTRACT

Silicon Nitride integrated photonic circuits have drawn much attention owing to its ultra-low loss and large Kerr nonlinearity. However, the lack of Pockels effect makes it difficult to be modulated electro-optically, which posts a major challenge for the further development of Si_3N_4 circuits with advanced functions. The widely adopted thermo-optical tuning suffers from large power consumption and restricted speed (\sim 1 kHz). In this study, microwave frequency modulation (up to 9 GHz) of Si_3N_4 ring resonator is achieved by exciting bulk acoustic waves piezoelectrically, which modulates the microring via stress-optical effect. The acoustic waves are confined tightly in a released SiO_2 thin film which enhances the acoustic energy density and thus modulation efficiency.

KEYWORDS

Acousto-optic modulator; Released HBAR; Si₃N₄ microring.

INTRODUCTION

Chip-scale monolithic photonics has grown rapidly in recent years due to applications ranging from atomic clocks [1], ultra-fast ranging [2], and broadband optical WDM networks [3]. Among these, Si₃N₄ photonic circuit has played an indispensable role due to its large refractive index, ultra-low loss from visible to mid-infrared, and large Kerr nonlinearity $\chi^{(3)}$ [4]. These features together endow Si₃N₄ with widespread applications, such as dissipative Kerr soliton microcomb generation [5], supercontinuum generation [6], and optical gyroscopes [7]. Yet, the absence of $\chi^{(2)}$ nonlinearity presents a major challenge for it to achieve fast tuning and modulation, which is usually required for Kerr microcomb feed-back control [8], optical nonreciprocity via spatiotemporal modulation [9], to name a few.

Currently, thermal-optical tuning [10] is usually employed when tuning is unavoidable. However, the long thermal response time restricts the speed to ~kHz, and the high power consumption (~10 mW) and thermal crosstalk prevent large scale integration and cryogenic applications [11]. Because of that, many efforts have been done by hybrid integration with electro-optical materials lead zirconate titanate (PZT) [12], lithium niobate (LiNbO₃) [13] and 2D materials (graphene [14], monolayer WS₂ [15]), at the expenses of lower optical Q, fabrication complexity, and dispersion engineering for comb generation.

Acousto-optic modulation (AOM) via photoelastic and moving boundary effects has been widely explored as a result of the maturity of Micro-Electro-Mechanical Systems (MEMS) and nano-fabrication technologies.

Microwave frequency modulation through exciting surface acoustic waves (SAW) has been applied successfully onto optical materials like AlN [16], LiNbO $_3$ [17], and Si [18]. When applying SAW AOM to Si $_3$ N $_4$ system, there presents one engineering problem for the trade-off between modulation efficiency and preserving low waveguide losses. As a nature of the SAW, the acoustic wave energy attenuates fast from the surface to the substrate, especially when going beyond GHz frequencies. This requires the waveguides to be within sub-micron away from the surface [18]. However, this insufficient cladding thickness compromises the low-loss of Si $_3$ N $_4$ waveguides, which is one of the main advantages of Si $_3$ N $_4$ photonics.

Most recently, we reported the AOM of Si₃N₄ microring using high-overtone bulk acoustic wave resonances (HBAR) [19], where the acoustic wave transmits vertically towards the substrate. This releases a degree of freedom for the design from the surface to out of the plane, where the waveguide can be buried deeply in a thick cladding layer. This largely preserves waveguide low-losses and large optical O of the Si₃N₄ ring resonator. Also, the acoustic resonances primarily rely on the material stack and thickness rather than lithography, which gives more lateral design freedoms regarding footprint, actuator shape, and fabrication cost, compared with SAW. Additionally, the high vertical acoustic mode confinement helps keep low cross-talk between two closely adjacent actuators, which is advantageous for compact spatiotemporal modulation [19].

However, the HBAR AOM is still suffering from low modulation efficiency which is mainly limited by the electromechanical and optomechanical coupling efficiency. In the previous study, the acoustic wave is evenly distributed over the whole 200 µm Si substrate which lowers acoustic excitation efficiency, and the large mode volume decreases optomechanical coupling rate g₀ [19]. Here, we remove the Si substrate by forming a freestanding 5.5 µm SiO₂ membrane where the bulk acoustic waves are tightly confined. The overall efficiency is increased by two orders of magnitudes, and AOM is observed up to 9 GHz, which enters into microwave Xband. This high-frequency AOM of Si₃N₄ will find widespread applications such as injection-locking of Kerr combs with 10 GHz FSR [20], atomic clocks that use Cesium's 9.19 GHz hyperfine transition frequency as a reference [21].

DEVICE DESIGN

Figure. 1(a) shows the optical image of the fabricated device with Aluminum Nitride (AlN) actuators sitting on a released oxide membrane that is anchored at the outer edge. The optical microring is located at the inner

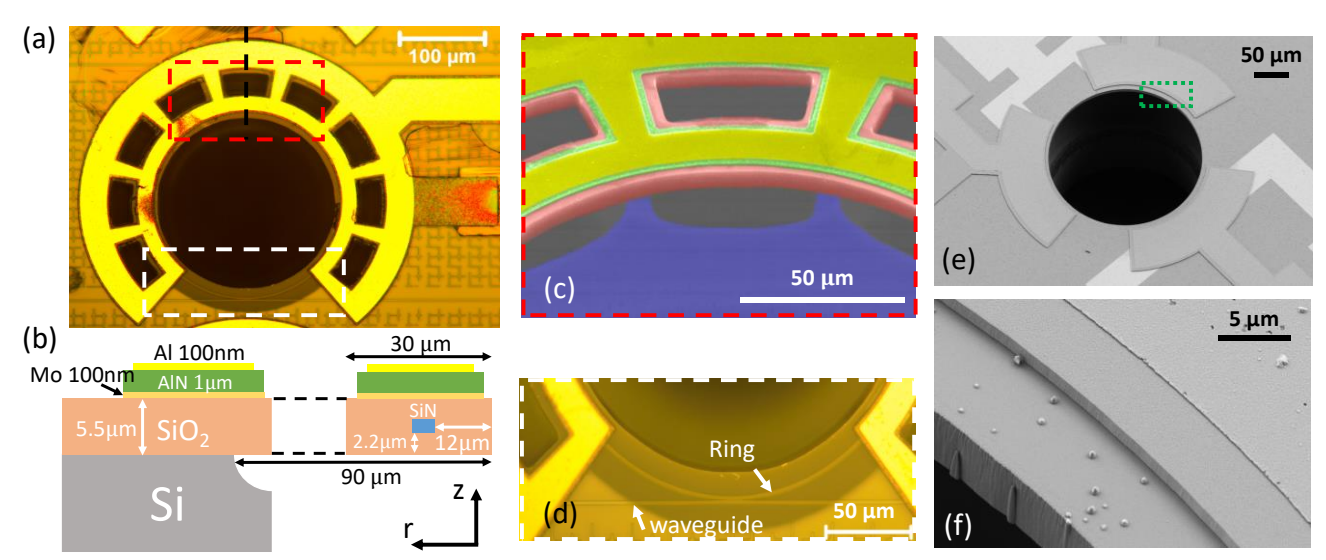


Figure 1: (a) Optical microscope of the fabricated device. (b) Schematic of cross-section of the device along the black dashed line in (a). The critical dimensions are as labeled. (c) False color SEM of the red box region in (a), illustrating AlN (green) film with Al (yellow) electrode on oxide (red) membrane. Blue is the etched Si substrate. (d) Zoom-in optical image of the bus waveguide coupling region as in the white box region in (a), showing the position of microring relative to the actuator. (e) SEM of another device with three actuators fabricated on the same optical ring. (f) Zoom-in SEM of region in green box in (e).

periphery. There are 9 rectangle holes inside the membrane defined for uniform release. The cross-section is illustrated in Fig. 1(b). 1 μm AlN piezoelectric film is sandwiched between top Aluminum and bottom Molybdenum electrodes, each with 100 nm. The Si $_3$ N $_4$ waveguide (0.8x1.8 μm^2) is embedded inside 5.5 μm SiO $_2$ cladding and is 2.5 μm away from the bottom electrode which reduces the absorption from Mo and scattering from layer interfaces. Also, the waveguide sits 12 μm away from the inner edge for better overlap with the piezoelectric actuator and preventing the scattering from sidewall roughness due to oxide etching. The radius of the optical ring is 118 μm . The fabrication procedure can be found in our previous work [22].

The free-standing membrane can be seen more clearly from the skewed false-color SEM in Fig. 1(c). To protect coupling between the waveguide and the ring from being perturbed by piezoelectric actuation, there is an opening region around the coupling area without any metal and piezoelectric material [Fig. 1(d)]. As we vibrate the AlN film by applying sinusoidal electrical signals to the electrodes, an acoustic wave is launched vertically into the SiO2 membrane. The smooth and flat top and bottom surfaces of the oxide layer forms an acoustic Fabry-Pérot cavity that confines acoustic energy and form a series of acoustic resonances. The generated stress and deformation modulates the optical waveguide's index through photoelastic and moving boundary effects. The acoustic waves are confined tightly in the vertical direction which helps to fabricate multiple actuators on the same optical microring in a compact form, as shown in Fig. 1(e). This would enable spatio-temporal modulation as required by optical nonreciprocal devices

ELECTROMECHANICAL RESPONSE

At first, the electromechanical response is

characterized by measuring the electrical reflection S₁₁ using port 1 of the vector network analyzer (VNA) [see Fig. 2(a)], which shows up the energy conversion from electrical to mechanical vibration as a dip. The result is shown in Fig. 2(b) where a series of periodic resonances can be observed with a free spectrum range (FSR) of 490 MHz. The mode order for each HBAR resonance is as labeled, which corresponds to the number of wavelengths in one round-trip inside the cavity as in any Fabry-Pérot cavity. This can be seen more clearly from the Finite Element (COMSOL) simulations of the stress distribution for two typical modes at 1.8 GHz and 4 GHz in Fig. 2(d). Since the stress distributes uniformly over the whole oxide membrane, the optical waveguide can be buried deep inside the cladding without compromising the modulation efficiency.

Interestingly, the electromechanical response is enhanced (deeper resonance) around 4 GHz as in the green shaded region. This is because, at this frequency, the half acoustic wavelength in AlN equals the AlN thickness, approaching the fundamental (1st order) resonance of the AlN cavity [see mode simulation of order 9 in Fig. 2(d)]. Besides the sharp resonances, there are small periodic dips overlapped at the background with a much smaller FSR of 17 MHz [see the zoom-in shown in Fig. 2(b) inset]. This comes from the HBAR resonances from the Si substrate as part of the contact pads and traces are not fully released and sits on the rigid substrate [19]. By having a rough backside substrate surface, these resonances can be avoided in the future, which will prevent the energy leak into the substrate and increase the mechanical O.

The electromechanical coupling efficiency $k^2_{t,eff}$ for each mode is calculated using the traditional Mason model as shown in Fig. 2(c). The efficiency gradually increases as the frequency approaches the AlN fundamental resonance. A maximum of 2% can be

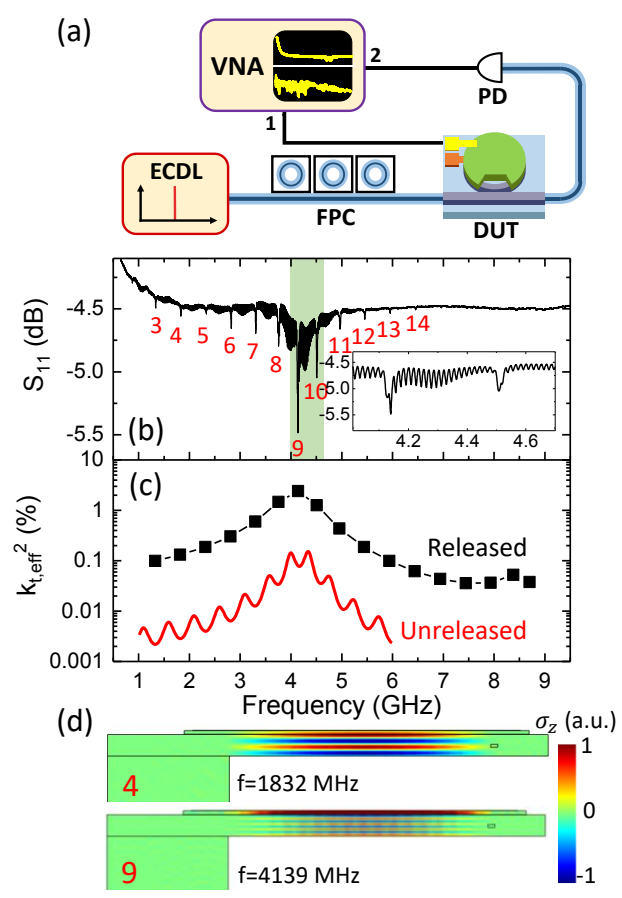


Figure 2: (a) Schematic of the setup for measuring electromechanical and optomechanical response. ECDL: external cavity diode laser, FPC: fiber polarization controller, DUT: device under test, PD: photo-diode, VNA: vector network analyzer. (b) Electromechanical S_{11} spectrum from 1 to 10 GHz with the mode order labeled for each visible acoustic resonance in oxide cavity. The inset shows the zoom-in of the green shaded region. (c) Calculated electromechanical coupling efficiency $k^2_{t,eff}$ for each HBAR mode (black square). The $k^2_{t,eff}$ of unreleased HBAR (red curve) is plotted for comparison. (d) Numerical simulation of the vertical stress distribution σ_z for two typical modes. The scale bars are normalized by maximum stress.

achieved which is one order of magnitude improvement over previous HBAR modes with giant Si substrate [red curve in Fig. 2(c)] [19]. It can be seen that there is also an efficiency enhancement around 8.5 GHz which corresponds to the second order resonance of the AlN film. Theoretically, the second order AlN resonance can hardly be observed if the structure is symmetric with respect to the AlN film, since the net stress generated in the piezoelectric film is zero [23]. However, the symmetry is broken due to the choice of different materials as top and bottom metals and biasing of oxide layer. We will see below the second harmonic resonance will enhance the modulation at that high frequencies.

OPTOMECHANICAL RESPONSE

As aforementioned, each of the HBAR modes can be excited to modulate the optical refractive index via the stress-optical effect. This is measured by performing

optomechanical S_{21} measurements, where, by setting the input laser frequency (~1550 nm) at the slope of the optical resonance, the output modulated laser intensity is detected by a high-speed photodetector (PD) and sent to port 2 of the VNA, while a -5 dBm RF signal from port 1 of the VNA is launched on the AlN actuator [see Fig. 2(a)]. From Fig. 3 one can see the resonant modulation peaks corresponding to each of the oxide HBAR modes from S_{11} . The small resonances from Si substrate HBAR as presented in S_{11} do not show up in optomechanical S_{21} , since the Si HBAR mainly locates at the outer anchor region which is far away from the inner Si_3N_4 ring.

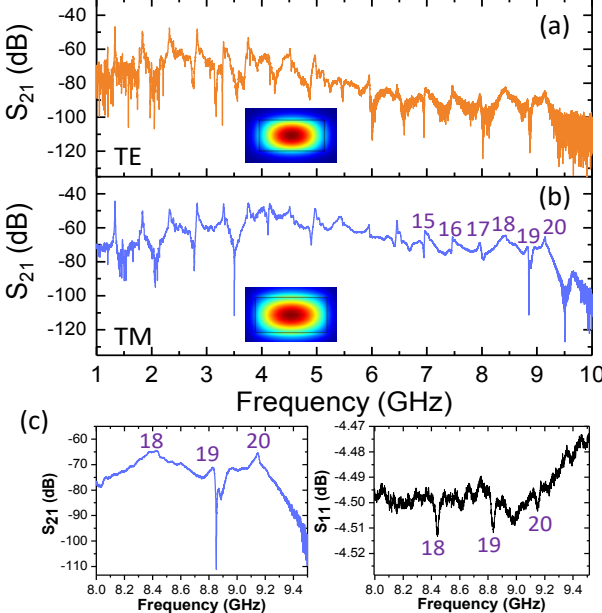


Figure 3: Acousto-optic modulation response S_{21} for (a) TE and (b) TM modes from 1 to 10 GHz. Periodic resonances can be observed corresponds to each of the dip from S_{11} . The orders for the resonances at high frequencies that can hardly be distinguished in S_{11} are as labeled. The simulated TE and TM optical modes are as shown in the insets. (c) Zoom-in S_{21} of TM mode (left) and S_{11} (right) around 9 GHz.

Intriguingly, resonances up to 9.15 GHz can be resolved, as shown in Fig. 3(c). Although the resonances of modes from 15 to 20 are very weak in S₁₁ [Fig. 3(c)], the optomechanical response shows a large signal to noise ratio (SNR) thanks to the high optical sensitivity. This is true for both TE and TM modes, although TE shows lower level responses at high frequencies due to its higher optical Q and thus longer response time. The second-order resonance from AlN film helps to enhance the modulation efficiency at high frequencies around 9 GHz.

As high as -45dB direct transduction efficiency from input RF to photodetector output at 4 GHz is achieved, which is two orders of magnitude increased compared with previous unreleased HBAR AOM under the similar input optical intensity (~100 μW). As mentioned earlier, one order of magnitude improvement comes from the electromechanical coupling efficiency. The other one order is from the enhancement of optomechanical coupling rate g_0 due to the shrink of mechanical mode volume.

In conclusion, the acousto-optic modulation of Si₃N₄

microring resonator is demonstrated by up to 9.15 GHz. This frequency is close to the 9.19 GHz transition frequency of Cesium which is usually adopted as the frequency reference in atomic clocks. Since the mechanical resonance frequency is mainly determined by the layer thicknesses, it can be controlled more precisely and uniformly over the whole wafer as compared with submicron interdigital transducer fingers of using SAW AOM. This could help reduce fabrication costs and improve yield. Also, since the whole optical circuits are embedded in the SiO₂ film, the coupling gap between waveguide and ring is protected from vibration which would otherwise introduce extra noises.

Due to the better mechanical mode confinement, the modulation efficiency shows two orders of magnitude improvement over unreleased devices. The implementation of efficient AOM will bring novel features and functionalities into Si₃N₄ photonics, and advanced applications can be foreseen, such as in chipscale atomic clocks, topological photonics, and optical spectroscopy.

ACKNOWLEDGEMENTS

The authors would like to thank Swiss National Science Foundation No. 176563 (BRIDGE); Defense Projects Agency Advanced Research (DARPA), Microsystems Technology Office (MTO), No. HR0011-15-C-0055 (DODOS); European Union's H2020 research and innovation program, FET Proactive Grant No. 732894 (HOT); NSF Award No. 1839164 (RAISE-TAOS); NSF QISE-NET under grant DMR 17-47426. Samples were fabricated in the EPFL center of MicroNanoTechnology (CMi), and Birck Nanotechnology Center at Purdue University. The authors would like to thank Mohammad Bereyhi and Dr. Ben Yu for valuable discussion, and Bin Dong and Michael Zervas for fabricating the device.

REFERENCES

- [1] Z. L. Newman *et al.*, "Architecture for the photonic integration of an optical atomic clock," *Optica*, vol. 6, no. 5, pp. 680–685, 2019.
- [2] P. Trocha *et al.*, "Ultrafast optical ranging using microresonator soliton frequency combs," *Science* (80-.)., vol. 359, no. 6378, pp. 887–891, 2018.
- [3] J. Pfeifle *et al.*, "Coherent terabit communications with microresonator Kerr frequency combs," *Nat. Photonics*, vol. 8, no. 5, pp. 375–380, 2014.
- [4] D. J. Moss, R. Morandotti, A. L. Gaeta, and Lipson Michal, "New CMOS-compatible platforms based on silicon nitride and Hydex for nonlinear optics," *Nat. Photonics*, vol. 7, no. 8, pp. 597–607, 2013.
- [5] T. J. Kippenberg, R. Holzwarth, and S. A. Diddams, "Microresonator-based optical frequency combs.," *Science*, vol. 332, no. 6029, pp. 555–9, 2011.
- [6] A. L. Gaeta, M. Lipson, and T. J. Kippenberg, "Photonic-chip-based frequency combs," *Nat. Photonics*, vol. 13, no. 3, pp. 158–169, 2019.
- [7] S. Gundavarapu *et al.*, "Interferometric Optical Gyroscope Based on an Integrated Si 3 N 4 Low-Loss Waveguide Coil," *J. Light. Technol.*, vol. 36, no. 4, pp. 1185–1191, 2018.

- [8] J. Liu *et al.*, "Monolithic piezoelectric control of soliton microcombs," *Nature*, vol. 583, no. 7816, pp. 385–390, 2020.
- [9] Y. Shi, Q. Lin, M. Minkov, and S. Fan, "Nonreciprocal Optical Dissipation Based on Direction-Dependent Rabi Splitting," *IEEE J. Sel. Top. Quantum Electron.*, vol. 24, no. 6, 2018.
- [10] C. Joshi *et al.*, "Thermally controlled comb generation and soliton modelocking in microresonators," *Opt. Lett.*, vol. 41, no. 11, pp. 2565–2568, Jun. 2016.
- [11] G. Moille *et al.*, "Kerr-Microresonator Soliton Frequency Combs at Cryogenic Temperatures," *Phys. Rev. Appl.*, vol. 12, no. 3, p. 1, 2019.
- [12] K. Alexander *et al.*, "Nanophotonic Pockels modulators on a silicon nitride platform," *Nat. Commun.*, vol. 9, no. 1, p. 3444, 2018.
- [13] A. N. R. Ahmed, S. Shi, M. Zablocki, P. Yao, and D. W. Prather, "Tunable hybrid silicon nitride and thin-film lithium niobate electro-optic microresonator," *Opt. Lett.*, vol. 44, no. 3, pp. 618–621, 2019.
- [14] B. Yao *et al.*, "Gate-tunable frequency combs in graphene--nitride microresonators," *Nature*, vol. 558, no. 7710, p. 410, 2018.
- [15] I. Datta *et al.*, "Low-loss composite photonic platform based on 2D semiconductor monolayers," *Nat. Photonics*, vol. 14, no. 4, pp. 256–262, 2020.
- [16] S. A. Tadesse and M. Li, "Sub-optical wavelength acoustic wave modulation of integrated photonic resonators at microwave frequencies," *Nat. Commun.*, vol. 5, p. 5402, 2014.
- [17] L. Shao *et al.*, "Microwave-to-optical conversion using lithium niobate thin-film acoustic resonators," *Optica*, vol. 6, no. 12, p. 1498, 2019.
- [18] E. A. Kittlaus, W. M. Jones, P. T. Rakich, N. T. Otterstrom, R. E. Muller, and M. Rais-Zadeh, "Electrically-driven Acousto-optics and Broadband Non-reciprocity in Silicon Photonics," arXiv Prepr. arXiv2004.01270, 2020.
- [19] H. Tian *et al.*, "Hybrid integrated photonics using bulk acoustic resonators," *Nat. Commun.*, vol. 11, no. 1, 2020.
- [20] J. Liu *et al.*, "Photonic microwave generation in the X- and K-band using integrated soliton microcombs," *Nat. Photonics*, vol. 14, no. 8, pp. 486–491, 2020.
- [21] C. T.-C. Nguyen and J. Kitching, "Towards Chip-Scale Atomic Clocks," in *ISSCC*. 2005 IEEE International Digest of Technical Papers. Solid-State Circuits Conference, 2005., 2005, no. 7, pp. 84–85.
- [22] B. Dong, H. Tian, M. Zervas, T. J. Kippenberg, and S. A. Bhave, "PORT: A piezoelectric optical resonance tuner," in 2018 IEEE Micro Electro Mechanical Systems (MEMS), 2018, pp. 739–742.
- [23] W. Pang, H. Zhang, R. C. Ruby, H. Yu, and E. S. Kim, "Analytical and experimental study on the second harmonic mode response of a bulk acoustic wave resonator," *J. Micromechanics Microengineering*, vol. 20, no. 11, p. 115015, 2010.

CONTACT

*Sunil A. Bhave, mobile:1-510-390-3269; bhave@purdue.edu